

OPEN

Bridging functional and anatomical neural connectivity through cluster synchronization

Valentina Baruzzi¹, Matteo Lodi¹, Francesco Sorrentino² & Marco Storace¹✉

The dynamics of the brain results from the complex interplay of several neural populations and is affected by both the individual dynamics of these areas and their connection structure. Hence, a fundamental challenge is to derive models of the brain that reproduce both structural and functional features measured experimentally. Our work combines neuroimaging data, such as dMRI, which provides information on the structure of the anatomical connectomes, and fMRI, which detects patterns of approximate synchronous activity between brain areas. We employ cluster synchronization as a tool to integrate the imaging data of a subject into a coherent model, which reconciles structural and dynamic information. By using data-driven and model-based approaches, we refine the structural connectivity matrix in agreement with experimentally observed clusters of brain areas that display coherent activity. The proposed approach leverages the assumption of homogeneous brain areas; we show the robustness of this approach when heterogeneity between the brain areas is introduced in the form of noise, parameter mismatches, and connection delays. As a proof of concept, we apply this approach to MRI data of a healthy adult at resting state.

The complex spatio-temporal patterns of activity exhibited by the brain derive from the interplay between the neural dynamics of cortical areas and their connectivity. From a modeling standpoint, one of the most challenging problems is the inference of network parameters in a brain model to reproduce empirically observed activity, namely the so-called inverse problem¹. One of the pillars for deriving reliable models that under specific conditions can reproduce experimentally observed human brain functions is the growing availability of neuroimaging techniques, which allow the detection of patterns of activity across neural units that encode objects, concepts, or states of information². Various techniques based on imaging data have been developed to extract functional and structural connectivity matrices of the human/animal cortex, but the way brain function is shaped by the underlying anatomical substrate is far from being understood³. Moreover, despite its widespread use to probe the structural connectivity of the brain in both clinical and basic neuroscience, dMRI fiber tractography produces anatomical connectomes subject to quite a large degree of uncertainty, due to well-known pitfalls of this technique in terms of anatomical accuracy⁴. A second research path that is attracting a growing interest is how to employ network theory and nonlinear dynamics to build brain models based on imaging data^{5–12}.

The orchestrated activity of neural populations has been postulated to be one of the key mechanisms underlying brain functions¹³. At a microscopic level, individual neurons exhibit hardly predictable firing rates, with a non-negligible stochastic component¹⁴. At a macroscopic level, however, we see the emergence of regular oscillations of the local field potential (LFP) in specific brain areas, including one or more populations, such as in the case of the cortical rhythms in the cerebral cortex¹⁵. We do not observe complete (or identical) synchronization between brain areas, i.e., a situation in which all variables of all areas converge to the same dynamical state; synchronization is usually only approximate, with brain areas behaving coherently, and transient, with synchronized communities reoccurring intermittently in time and across scanning sessions¹⁶. One of the most common ways to non-invasively detect the presence of coherence among brain areas is to analyze the correlation between the blood oxygen level-dependent (BOLD) signals measured in these areas through functional magnetic resonance imaging (fMRI).

It is commonly agreed that brain functions strongly depend on anatomy, other than neural dynamics. Various efforts have been made to determine if functional connectivity and structural connectivity can be predicted from each other¹⁷: data-driven statistical models^{18–20} that do not assume any specific mode of interaction among neuronal populations; models emerging from network science and telecommunication engineering²¹ that conceptualize functional interactions as the superposition of elementary signaling events on the underlying anatomical

¹DITEN, University of Genoa, Via Opera Pia 11a, 16145 Genova, Italy. ²Mechanical Engineering Department, University of New Mexico, Albuquerque, NM 87131, USA. ✉email: marco.storace@unige.it

network; biophysical dynamical models^{22–24} that describe the collective dynamics of a neuronal ensemble in terms of their mean firing rate, which capture both local fluctuations and influence from other connected regions, and exhibit a rich repertoire of oscillations, synchrony, and waves. Many studies have investigated whether and how resting-state functional connectivity can be inferred from experimentally measured structural connectivity^{22,24,25}, and have found that strength, persistence, and spatial statistics of functional connections are constrained by the large-scale anatomical structure of the human cerebral cortex. Some studies have also proposed analytical approaches to derive linear relationships between functional and structural connectivity matrices, based on neural field theory²⁶ and spectral graph theory²⁷.

In this paper, we investigate an approach to reconcile information about structural connectivity and information on synchronous clusters obtained from fMRI data. Our proposed method provides a biophysical dynamical model in terms of a network, composed of weighted links and nodes representing brain areas. The network links (i.e., its topology) and weights are derived from an optimized version of the original structural connectivity matrix, obtained by imposing the network emergent dynamics to be compatible with the synchronous clusters evidenced by fMRI scans. The results are robust with respect to heterogeneity in the parameters of both network and nodes, the presence of noise, and connection delays. The main novelty element of this paper is the connection we establish between anatomical and functional data based on the study of cluster synchronization at different granularities. To the best of our knowledge, the concepts of cluster synchrony and equitable partitions have not been previously leveraged to relate the functional and structural connectomes of the brain.

As a proof of concept, we apply the method to public data obtained from 10 fMRI and 10 dMRI scans executed across a month of one healthy adult at resting state. Results obtained for two additional subjects of the same public dataset are provided in “Supplemental Material”, Note 2, and are aligned with the results presented here.

Results

Proposed method

The proposed method leverages structural and functional data in the form of connectivity matrices. In particular, structural connectivity matrices aggregate the information on fiber density between the different areas considered as network nodes; this information is derived from fiber tractography reconstruction techniques, which allow assessing the presence of neural tracts from dMRI data. Functional connectivity matrices aggregate the information on the correlation between the BOLD signals measured in the different areas through fMRI.

Nonlinear dynamics provides tools for studying complete cluster synchronization^{28–30}; when applying these tools to experimental data, for which synchronization is only approximate, a convenient first-order assumption is to deal with homogeneous nodes. On the one hand, this could be unrealistic, because in a real neuronal network each area is expected to be unique, i.e., from a modeling standpoint, to have its own parameter values, as the corresponding neuronal populations are heterogeneous with respect to multiple physical properties. On the other hand, the identification of these heterogeneities (and corresponding model parameters) from measured data is highly nontrivial and depends on the quality and quantity of data, the noise inherent to measurements of biological systems, and the complexity of the chosen model.

Figure 1 illustrates the main elements of the proposed method, which starts from functional and structural connectomes derived from fMRI and dMRI scans, respectively. The functional data evidences the presence of approximate synchronization (namely, high correlation) between the neural activity of specific brain areas. The areas with high correlation are assumed to be part of the same *synchronous cluster*. In order to reduce the uncertainty on the weights of the structural connectome⁴ we look for network models, with different granularity/resolution in terms of clusters, that are compatible with the clusters evidenced by the functional connectivity analysis. The key elements of the method are the following:

- We use the network *topology* defined by the structural connectome as a starting point.
- We use functional data to identify *clusters* of nodes with coherent activity through a hierarchical clustering algorithm, with multiple resolution levels.
- We add *dynamics* to the nodes through a neural mass model (NMM)³¹, choosing the network model to be *homogeneous* in the nodes, and focus the analysis on exact cluster synchronization; at this stage, we neglect higher-order model factors that pertain to the node features.
- We resort to the concept of equitable clusters^{32,33} in order to optimize the weights of the structural connectome with the aim of making the network compatible with the *existence* of clusters of highly functionally-correlated areas; this is done by changing the weights as little as possible from their experimentally measured values and by taking into account their measured uncertainty.
- We find a suitable range for a scale factor of the weights by applying the master stability function (MSF) approach³⁴ in order to ensure the *stability* of the compatible synchronous clusters.

After the steps above are taken, one can choose the model with the most suitable resolution level, according to the specific objective, and check the extent of the model robustness by reintroducing heterogeneity in either the connection weights and delays or the nodes. This leads to a set of perturbed models compatible with the data, in which both functional and anatomical connectivity are incorporated. We emphasize that the chosen unperturbed model is able to reproduce the correlation in the BOLD signals observed experimentally in fMRI data (i.e., the approximate synchronization between brain areas) with connection weights that differ from the dMRI connectivity matrix by an amount that is comparable with the uncertainty introduced by the measuring process.

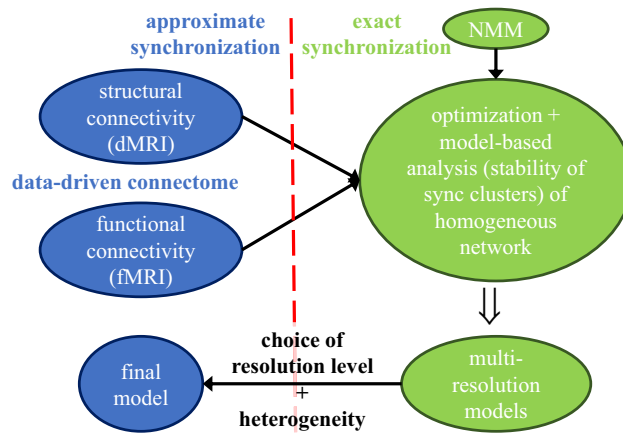


Figure 1. Summary of the proposed method. We start (top-left ovals) from data-driven structural (functional) connectomes, derived from dMRI (fMRI) scans. Each functional connectome evidences the correlation between the neural activity of different brain areas, and then the presence of approximately synchronized clusters, formed by areas with high correlation. There is a degree of uncertainty on the number of clusters the areas can be best aggregated into. Each structural connectome reflects the brain anatomy, with some uncertainty in the weight of each connection. Right (green) ovals: model-based method used to bridge functional and structural connectivity. The reference (homogeneous) network model has an initial topology defined by the structural connectome and node dynamics imposed by a NMM. The uncertainty on the clusters is managed through a multi-resolution approach, by analyzing different cluster partitions. For each resolution level, the uncertainty on the connection weights is reduced by optimizing them to enforce the existence of the cluster synchronous solution of that level. Bottom-left oval: one resolution level is chosen, and the corresponding model is made heterogeneous, thus obtaining again approximate synchronization.

Network model

We consider a weighted and undirected network graph with N nodes, each representing a cortical area. Edges represent long-range connections between the cortical areas. This graph can be described by a symmetric structural connectivity matrix A_0 , with entries a_{0ij} that are the connection weights. For a given subject, A_0 is built by normalizing and averaging the available M_d structural connectomes, which are measured in time periods that are short enough that anatomical connectivity at this scale does not vary significantly^{24,35}. Information on the uncertainty of each weight is stored in a matrix Σ_{A_0} , where each entry is the variance of the weight among the M_d normalized connectomes. A delay τ_{ij} is assigned to the connection between nodes i and j , according to the distance between the nodes and the propagation speed. By assigning dynamics to each node, the network of N coupled neural oscillators is described by the following general set of equations ($i, j = 1, \dots, N$):

$$\dot{\mathbf{x}}_i(t) = \mathbf{F}(\mathbf{x}_i(t)) + \boldsymbol{\Gamma} \left(\mathbf{x}_i(t), \sigma \sum_l \sum_j a_{ij}^l \mathbf{G}(\mathbf{x}_j(t - \tau^l)) \right) \quad (1)$$

where $\mathbf{x}_i \in \mathbb{R}^m$ are the state variables of node $i = 1, \dots, N$, $\mathbf{F} : \mathbb{R}^m \rightarrow \mathbb{R}^m$ describes the dynamics of an isolated node, $\boldsymbol{\Gamma} : \mathbb{R}^m \times \mathbb{R}^m \rightarrow \mathbb{R}^m$ describes the coupling between nodes, and a_{ij} is the strength of the coupling from node j to node i . The parameter σ controls the overall strength of the connections and $\mathbf{G} : \mathbb{R}^m \rightarrow \mathbb{R}^m$ is the coupling function. The delays τ_{ij} are quantized over L values τ^l , with $l = 1, \dots, L$. This quantization is necessary for computational purposes, and fully heterogeneous delays will be reintroduced *a posteriori*.

Identification of clusters of nodes with coherent activity

The functional connectomes refer to the same N brain areas and are in the form of correlation matrices, in which each entry describes the pair-wise temporal correlation between the activity of two brain areas. Given M_f functional connectomes measured from the same subject in the same conditions, it is possible to identify the clusters of nodes that exhibit coherent activity through a hierarchical clustering approach, as commonly done in the literature^{36–39}. Hierarchical clustering is applied to each functional connectome, and the resulting partitioning can be visualized as a dendrogram, an example of which is shown in Fig. 2 (see Methods for details).

A certain variability across the dendograms obtained from different fMRI sessions is expected. We aim to identify the set of node partitions that best describes the functional connectivity of the subject at different scales (i.e., at different levels ℓ of the dendrogram); to this end, we define the similarity index $\Psi_1(\ell)$, which measures the consistency of clusterings at different levels ℓ across the M_f fMRI sessions. The local maxima of $\Psi_1(\ell)$ allow selecting M_ℓ levels ℓ_k^* (each one cutting k branches of the dendrogram, thus identifying k clusters), which are collected in a set $\mathcal{L}^* = \{\ell_k^*\}$ (see Fig. 3a). The reference fMRI session s^* is identified through the similarity index $\Psi_2(s)$, which provides an indication of how much the clustering obtained from a session is similar to the clusterings from all other sessions; s^* is chosen as the maximum value of $\Psi_2(s)$ and the selected correlation matrix is referred to as X^* (see Fig. 3b). The similarity indices $\Psi_1(\ell)$ and $\Psi_2(s)$ are calculated by leveraging the Fowlkes and

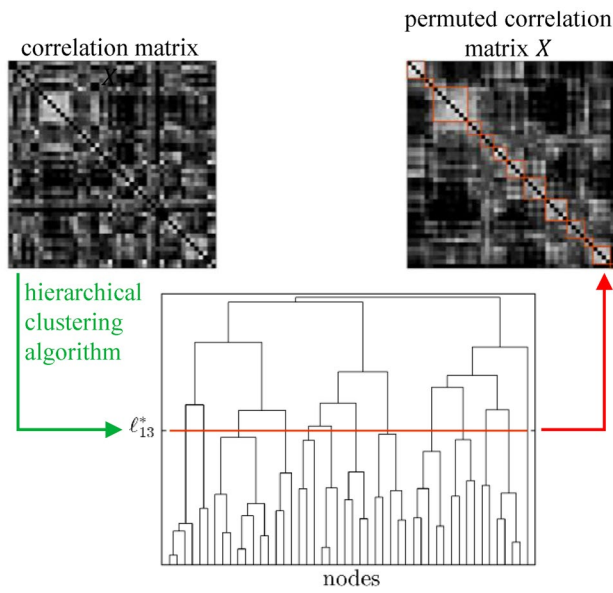


Figure 2. Given a correlation matrix, it is possible to identify the clusters of nodes that exhibit coherent activity with a hierarchical clustering approach. The obtained hierarchical clustering can be visualized in the form of a dendrogram, where nodes appear on the horizontal axis according to a permutation that places nodes belonging to the same cluster adjacent to one another. Depending on the level ℓ at which the dendrogram is cut horizontally, the corresponding clustering is described by the sub-trees originating from each branch cut by the line: for example, the red line cuts the dendrogram at the level corresponding to 13 clusters. The correlation matrix can be re-arranged based on the obtained permutation, so that the clusters can be evidenced along the diagonal.

Mallows method⁴⁰, which allows comparing two partitions by calculating the comparison measure $0 \leq B \leq 1$, as explained in detail in Methods.

To check if the structural connectivity matrix A_0 is already compatible with the clusters emerging from the analysis of functional data, for each level ℓ_k^* we simulate the network dynamics for an array of values of σ (see Eq. (1)) and different initial conditions; we then compute an average Fowlkes and Mallows matching index \bar{B} by comparing each partition obtained in simulation with the target partition associated with X^* . This procedure is detailed in Methods. If A_0 turns out to be inadequate to reproduce the clustering activity of the network (i.e., $\bar{B} \leq B_{th}$, with B_{th} user-defined threshold), we take the next steps of the method. We heuristically set $B_{th} = 0.7$.

Refining the structural connectivity matrix according to synchronized clusters

As a first approximation, we model the identified clusters of nodes with coherent activity as synchronized clusters. This model must admit these synchronized clusters as a stable synchronous solution. To impose this constraint, there are two distinct issues to be addressed: one is ensuring the existence of the desired cluster-synchronous solution, and the other one is ensuring its stability. The existence of a cluster-synchronous solution requires that, for proper initial conditions, nodes in the same cluster synchronize. This solution is also stable if, under small enough perturbations, the system state goes back to the same synchronous clusters.

We leverage here a fundamental principle: the existence of a particular set of self-sustained synchronized clusters in a network graph with homogeneous nodes can be ruled out or not based on the network topology, independently from the dynamical model of the nodes; in particular, the existence of an equitable partition for a given network is a necessary condition for the existence of a cluster synchronous solution^{41,42}. We remark that at this point we are only considering the existence of a cluster synchronous solution, not its stability; the possibility of convergence on such a solution depends also on the node dynamics, i.e., the functions \mathbf{F} and Γ in Eq. (1)⁴³.

Let us first consider the case with homogeneous delays, i.e. $L = 1$. A partition (and the corresponding coloring) is *equitable* if all nodes with color p receive the same overall input from the nodes of color q , for $p, q = 1, \dots, k$. For each level ℓ_k^* , given the set of target clusters, we want to obtain a structural connectivity matrix A_k for which they constitute an equitable partition.

The structural connectivity matrix A_0 is derived from diffusion MRI data, and, as such, it has positive entries, is symmetrical, and has null diagonal entries. The optimized matrix A_k is also constrained to (i) have positive entries, (ii) be symmetric, and (iii) have null diagonal entries, to maintain the original features of the structural connectivity matrix. From the variance matrix Σ_{A_0} , a ‘reliability’ matrix $\hat{\Sigma}_{A_0}$ is defined as $\hat{\Sigma}_{A_0} = \max(\Sigma_{A_0}) - \Sigma_{A_0} + \epsilon$, so that the entries with low variance have high reliability and vice versa; ϵ is an arbitrarily small quantity with the only function of avoiding zero entries. $\hat{\Sigma}_{A_0}$ is included in the cost function so that the more reliable an entry is, the less likely it is to be changed significantly in the optimization process to find A_k . The optimization process is as follows: the columns of A_k are stacked in the vector x ; the columns of the matrix obtained multiplying entry by entry A_0 by $\hat{\Sigma}_{A_0}$ are stacked in the vector α ; H is defined as the N^2

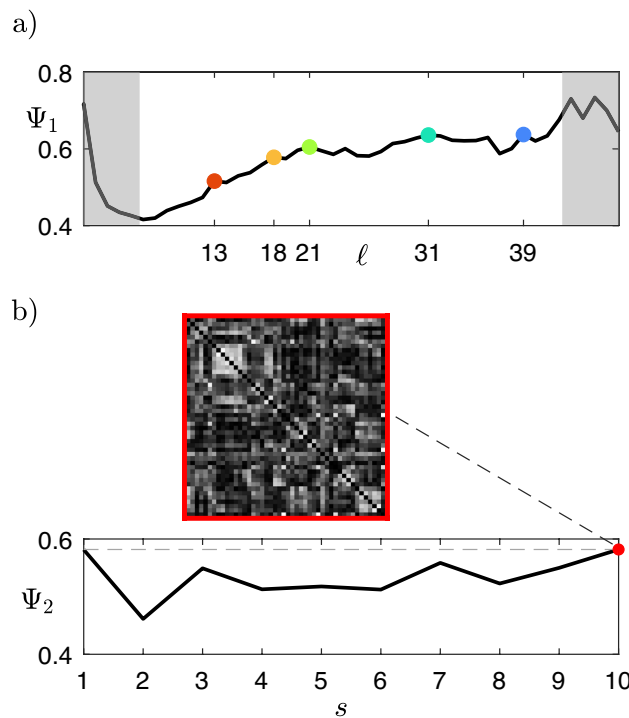


Figure 3. (a) Cumulative (across the 10 fMRI sessions) similarity index Ψ_1 , based on the Fowlkes and Mallows comparison measure, for each dendrogram level ℓ . Ψ_1 measures the consistency of the corresponding clustering across the fMRI sessions. Specific levels ℓ_k^* (corresponding to k clusters) are selected as local maxima of this curve (colored dots, same color code as in Figs. 5 and 6). We chose to discard local maxima that are not in ascending order and trivial partitions with too few or too many clusters (grey areas, corresponding to those in panel a) of Fig. 5). (b) Cumulative (across levels ℓ_k^*) similarity index Ψ_2 for each of the 10 sessions. Ψ_2 indicates how much the clustering obtained from a session is similar to the clusterings from all other sessions. The fMRI session corresponding to the maximum value of Ψ_2 (red dot, corresponding to the correlation matrix X^* shown above) is chosen as the most representative of the subject.

-size diagonal matrix with $\hat{\Sigma}_{A_0}$ entries on its diagonal; $M_1x = 0$ codifies the equitable partition conditions and $M_2x = 0$ codifies constraints (ii) and (iii). The optimal vector x (i.e., the matrix A_k) is found by solving the following optimization problem, with quadratic objective function and linear constraints, of equality and inequality:

$$\min_x \frac{1}{2} x^T H x - \alpha^T x \quad (2)$$

s.t.

$$\begin{aligned} x &> 0 \\ M_1x &= 0 \\ M_2x &= 0. \end{aligned} \quad (3)$$

This problem can be easily recast as a quadratic programming (QP) problem and numerically solved.

To carry out the optimization when delays τ_{ij} are quantized over multiple values (i.e. $L > 1$) the structural connectivity matrix A_0 is split into L matrices A_0^l , each corresponding to a coupling with delay τ^l . In particular, entries of A_0^l corresponding to different delays are set to 0 and $\sum_l A_0^l = A_0$. Each matrix A_0^l is optimized individually, thus obtaining matrices A_k^l , according to the definition of equitable partitions for graphs with L different kinds of couplings³⁰. The final optimized structural connectivity matrix for level k is obtained as $\sum_l A_k^l = A_k$. For high values of L , we would obtain extremely sparse matrices A_0^l , thus reducing the degrees of freedom for the optimization algorithm, since we constrain zero entries to be kept at zero.

Stability analysis through master stability function

The stability of the synchronous target clusters for each level ℓ_k^* is assessed by using the MSF approach³⁴. To illustrate this step of the proposed method, we refer to a network of N coupled Wilson-Cowan NMMs⁴⁴ (see Methods), which can be described by the general set of equations (1) with $m = 2$ state variables:

$$\begin{aligned}\mathbf{x}_i &= \begin{bmatrix} E_i \\ I_i \end{bmatrix}, \\ \mathbf{F}(\mathbf{x}_i) &= \begin{bmatrix} \frac{1}{\tau_E}(-E_i) \\ \frac{1}{\tau_I}(-I_i + \frac{1}{1+e^{-c(w_{EI}E_i-\theta)}}) \end{bmatrix}, \\ \Gamma(\mathbf{x}_i, \sigma \sum_j a_{ij} \mathbf{G}(\mathbf{x}_j)) &= \begin{bmatrix} \frac{1}{\tau_E} \frac{1}{1+e^{-c(w_{EE}E_i-w_{IE}I_i+p+E_i^{sym}-\theta)}} \\ 0 \end{bmatrix}, \\ \mathbf{G}(\mathbf{x}_j) &= \begin{bmatrix} E_j \\ 0 \end{bmatrix}.\end{aligned}$$

We can denote the cluster synchronization state as $\mathbf{x}_i(t) = \mathbf{s}_p(t)$, where node i belongs to cluster C_p . Small perturbations $\mathbf{w}_i(t) = \mathbf{x}_i(t) - \mathbf{s}_p(t)$, stacked in the state perturbation vector $\mathbf{W}(t)$, are introduced to investigate the stability of the synchronous state and their linearized variational equations are derived (see Methods for details).

We resort to a coordinate transformation based on simultaneous block diagonalization (SBD)^{45–48}, performed through the canonical transformation matrix $T = \begin{pmatrix} T_{\parallel} \\ T_{\perp} \end{pmatrix}$ ⁴⁹. An alternative to this method is the one proposed in⁵⁰. The $k \times N$ submatrix T_{\parallel} is associated with the directions *along* the synchronization manifold and the corresponding perturbations do not influence the stability of the synchronized clusters. The $(N-k) \times N$ submatrix T_{\perp} is associated with the directions *transverse* to the synchronization manifold and the evolution of the variational equation along these directions determines the stability of the synchronized clusters.

Transverse perturbations are denoted as $\boldsymbol{\eta}_{\perp}(t) = (T_{\perp} \otimes I_m)\mathbf{W}(t)$ (where \otimes is the Kronecker product and I_m is a $m \times m$ identity matrix) and their variational equation is:

$$\dot{\boldsymbol{\eta}}_{\perp}(t) = \rho_1(\{\mathbf{s}_p(t)\})\boldsymbol{\eta}_{\perp}(t) + \rho_2^l(\{\mathbf{s}_p(t)\})\boldsymbol{\eta}_{\perp}(t - \tau^l) \quad (4)$$

where the set $\{\mathbf{s}_p(\cdot)\}$ collects all the synchronous solutions corresponding to the k clusters and ρ_1 and ρ_2^l are time-varying matrices defined in Methods. The Lyapunov exponents for each $\boldsymbol{\eta}_{\perp}$ component are calculated and the σ intervals where the cluster synchronous solution is stable are determined as those where the maximum Lyapunov exponent (MLE) is negative.

Introducing heterogeneity in the network model

The assumption of exact cluster synchronization is restrictive and unrealistic when referring to experimental data from recorded brain activity. For this reason, we check if the obtained stability intervals of σ values hold also for perturbed versions of A_k that produce approximate synchronization. For small perturbation of the matrix A_k , this was studied in⁴². We repeat the compatibility check as described in the simulation procedure in Methods on the optimized structural connectivity matrices A_k perturbed by additive Gaussian white noise with mean 0 and standard deviation σ_A . This analysis tests for up to which level of noise on the connection weights the optimized structural connectivity matrix remains compatible with the target clusters, derived from the functional connectivity matrix, in the considered σ intervals.

Similar analyses can be carried out by adding a white Gaussian noise term $\eta_i(t)$ with standard deviation σ_{η} to every node's input or by introducing heterogeneous node parameters.

Proof of concept of the method

In this section, the method steps are illustrated through a case study. All functional and structural connectomes used in this study are part of the Neurodata MRI Cloud database⁵¹. They are produced with NeuroData's MRI Graphs pipeline⁵² from the HNU1 dataset⁵³, which includes $M_f = 10$ fMRI and $M_d = 10$ dMRI scans of 30 healthy adults at resting state collected over the span of one month. The illustrative example presented in this paper refers to subject 0025452, which showed the highest similarity index Ψ_1 averaged across levels.

First, we present the results for different clustering granularities for the case with no connection delays (i.e. $\tau_{ij} = 0 \quad \forall i, j$). Next, we analyze the case with delays τ_{ij} quantized over $L = 3$ values for an intermediate granularity level ℓ_k^* .

Network model

We consider a weighted and undirected network graph (described by the symmetric structural connectivity matrix A_0) with $N = 48$ nodes (Fig. 4), each representing a cortical area according to the Harvard-Oxford Cortical Atlas (HOA); a list of the cortical areas is provided in “Supplemental Material”, Note 1). Edges represent long-range connections between the cortical areas.

Identification of clusters of nodes with coherent activity

For each correlation matrix X , we define the corresponding dissimilarity matrix as $D = \mathbf{1}_N - X$ (where $\mathbf{1}_N$ is an $N \times N$ matrix with all entries equal to 1). D is converted to vector form with Matlab's *squareform* function and fed to Matlab's *linkage* function with the ‘complete’ option (which implements the farthest neighbor method) in order to perform the hierarchical clustering. In this case, we identify $\mathcal{L}^* = \{\ell_{13}^*, \ell_{18}^*, \ell_{21}^*, \ell_{31}^*, \ell_{39}^*\}$ (i.e., $k \in \{13, 18, 21, 31, 39\}$) as the set of local maxima of $\Psi_1(\ell)$, and maximum Ψ_2 for session $s^* = 10$ (see Fig. 3). The level ℓ_{13}^* (ℓ_{39}^*) corresponds to the coarsest (finest) scale of description of the brain areas' correlations.

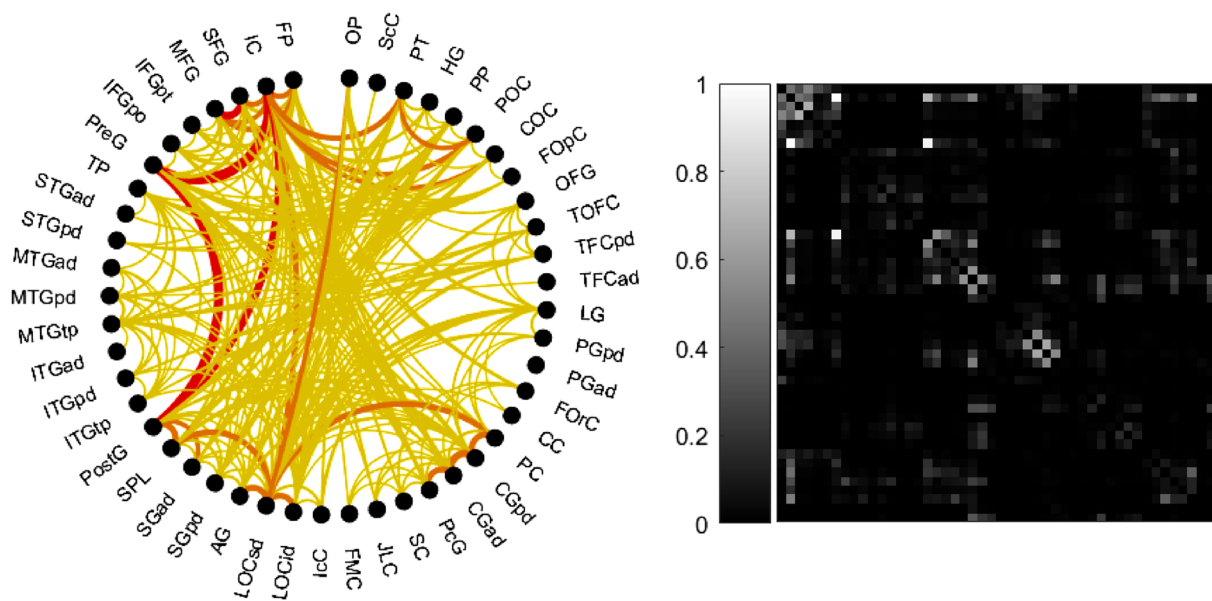


Figure 4. Connectogram (left) described by the structural connectivity matrix A_0 (right). For clarity, only 30 % of the edges (corresponding to the highest weights) are displayed. Edges are shown in yellow if the associated weight $a_{0ij} \in [0, 0.33]$, in orange if $a_{0ij} \in [0.33, 0.66]$, in red if $a_{0ij} \in [0.66, 1]$. Nodes are labeled according to the HOA. Connectogram graphed with SPIDER-NET software⁵⁴.

Panel a of Fig. 5 shows the dendrogram associated with X^* , where the levels ℓ_k^* are marked by colored horizontal lines. The sets of clusters corresponding to levels ℓ_{13}^* , ℓ_{18}^* , and ℓ_{31}^* are highlighted over the correlation matrix X^* in panel b. Nodes on the dendrogram are labeled according to the HOA and their division in clusters corresponding to ℓ_{13}^* is evidenced by red boxes at the bottom of panel a. Nodes belonging to the default mode network (DMN), the first and most studied resting-state subnetwork^{55–57}, are highlighted in yellow. We remark that we do not exploit neuroscientifically relevant a priori knowledge to identify the clusters, but only the functional connectivity matrices obtained from fMRI data. Nonetheless, we can observe that 5 out of the 8 cortical areas constituting the DMN, as listed in^{58,59}, belong to the same cluster (the frontal pole, the angular gyrus, and the posterior divisions of the supramarginal gyrus, the middle temporal gyrus and the superior temporal gyrus), 2 constitute the adjacent cluster (the posterior division of the cingulate gyrus and the precuneous cortex), and only 1 (the frontal medial cortex) is isolated. This shows that we observe coherent behavior among the majority of the cortical areas belonging to the DMN.

Is the structural connectivity matrix A_0 compatible with the clustering observed in the functional connectivity matrix X^* ? To verify this, we model the network nodes as Wilson-Cowan neural masses⁴⁴ and the BOLD signal associated with each node by using the Balloon-Windkessel hemodynamic model of Friston and Harrison⁶⁰. Details on the models and model parameters (set so that the nodes exhibit oscillatory behavior, in accordance with the local field potential gamma oscillations observed in cortical activity) can be found in Methods.

The initial conditions for all network simulations (performed with the *ode45* Matlab ODE solver) are set according to the following criteria: we want to give the same n_{IC} initial conditions to the nodes belonging to the same target cluster, to enable the emergence of said cluster; at the same time, we want to perturb slightly these initial conditions to ensure that the state variables do not get stuck on an unstable orbit. For this reason, the initial conditions for the state variables of the nodes belonging to the same target cluster are defined as a common mean value, set randomly at each trial, plus Gaussian noise with a small standard deviation of 10^{-5} . Initial conditions for the state variables of the BOLD model are simply set randomly at each trial, regardless of the target cluster configuration. The correlation matrices are calculated using Matlab's *corrcoef* function, which returns an $N \times N$ matrix with correlation coefficients of pairs of variables as off-diagonal entries.

In our case study, the average comparison measure \bar{B} is found to be low (always below 0.3) for all levels ℓ_k^* and for all values of σ , as shown in Fig. 6.

This highlights that using the information contained in the structural connectivity matrix A_0 ‘as is’ to model connection weights generates results that are incompatible with the observed functional connectivity. This finding is in agreement with other studies that have questioned the reliability of using connectivity matrices describing fiber density as a quantitative indication of connection weights^{61–63}. Next, we show how the proposed method refines the structural connectivity matrix A_0 to make it compatible with the observed functional connectivity.

Refining the structural connectivity matrix according to synchronized clusters

We apply the proposed optimization procedure, thus obtaining the new structural connectivity matrices A_k . For the sake of comparison, we define the matrix Ξ_k as the element-wise square difference between A_k and A_0 , i.e., $\Xi_{kj} = (a_{kj} - a_{0,j})^2$. For matrices Σ_{A_0} and Ξ_k we introduce, respectively, the permutations $p^{\Sigma_{A_0}}$ and p^{Ξ_k} of the linear index $i_\ell = i \cdot N + j$, which make the entries of the matrices ordered from the smallest to the largest. Fig. 7 (top panels) shows that the entries of the matrix Ξ_k plotted against the permuted linear index $p^{\Xi_k}(i_\ell)$ are

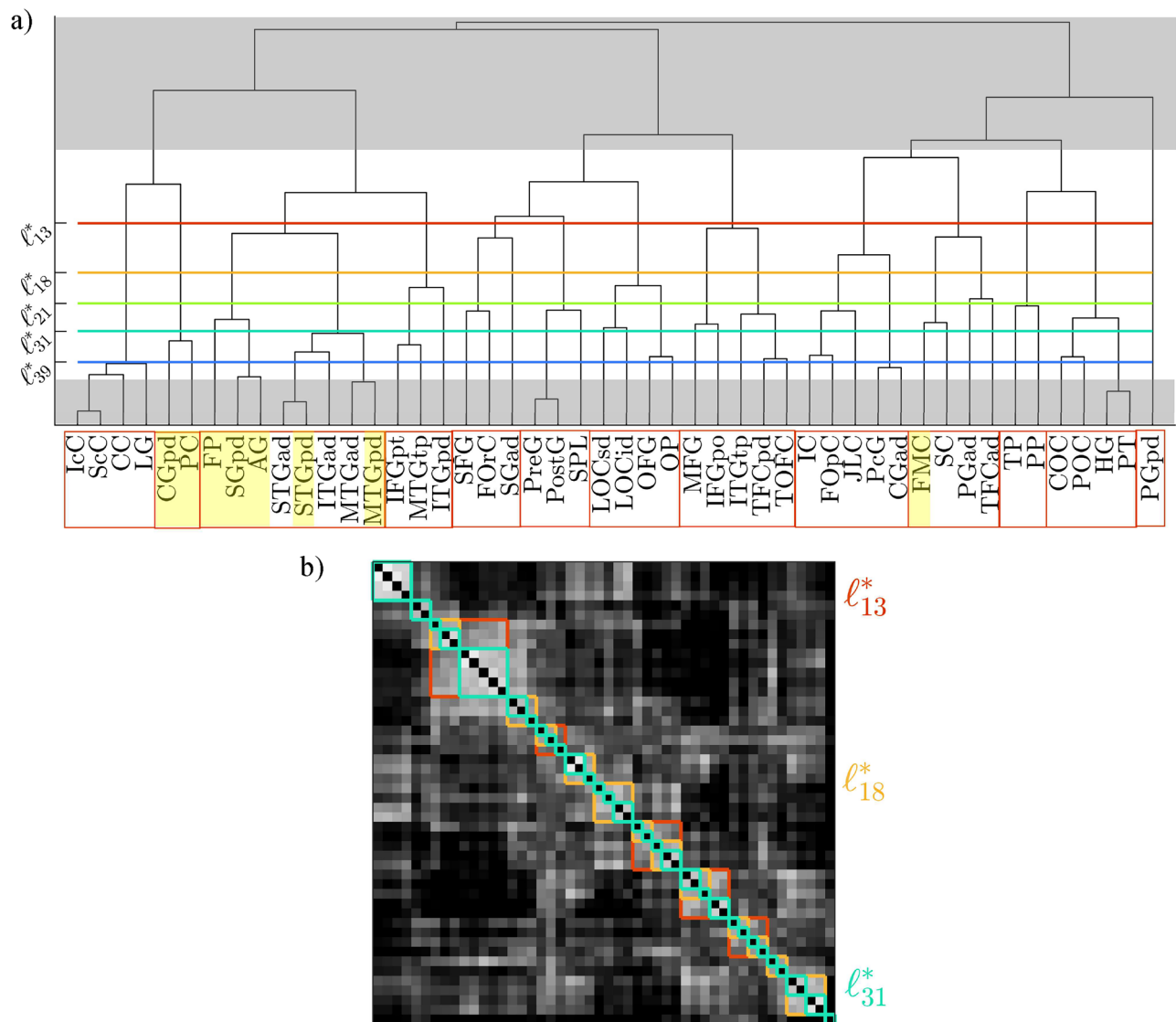


Figure 5. (a) Dendrogram associated with X^* . The levels ℓ_k^* are marked by colored horizontal lines. Grey areas correspond to trivial partitions with too few or too many clusters. Nodes are labeled according to the HOA and their division in clusters corresponding to ℓ_{13}^* is evidenced by red boxes. Nodes belonging to the DMN are highlighted in yellow. (b) Correlation matrix X^* where the sets of clusters corresponding to levels ℓ_{13}^* (red), ℓ_{18}^* (orange), and ℓ_{31}^* (teal) are highlighted.

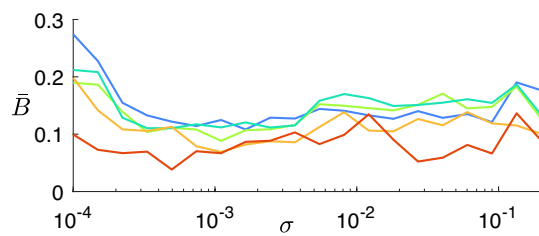


Figure 6. Comparison measure \bar{B} between the cluster partition obtained from network simulations with synaptic weights a_{0ij} (entries of A_0) and the target cluster partition associated with X^* , averaged over 30 random trials for different values of σ . Different colors refer to different levels ℓ_k^* .

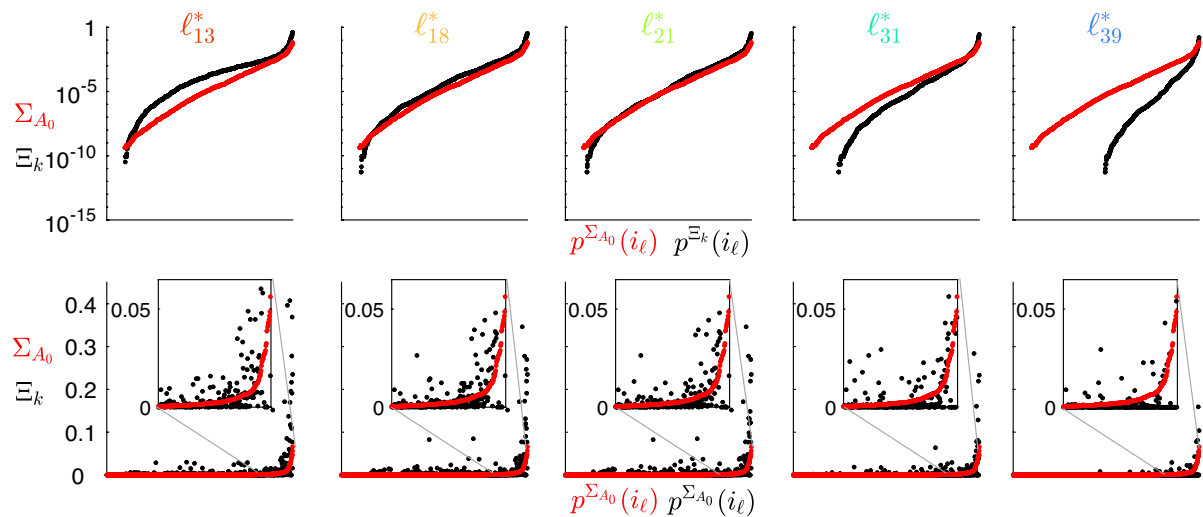


Figure 7. Entries of the matrices Σ_{A_0} (red dots) and Ξ_k (black dots), for all levels ℓ_k^* . Top panels: entries of both Σ_{A_0} and Ξ_k are displayed from the smallest to the largest and are plotted on a semi-logarithmic scale, with their linear indices i_ℓ ordered according to permutations $p^{\Sigma_{A_0}}$ and p^{Ξ_k} , respectively. Bottom panels: entries of Σ_{A_0} are displayed on a linear scale from the smallest to the largest, with their linear indices i_ℓ ordered according to permutation $p^{\Sigma_{A_0}}$; entries of Ξ_k are displayed following the same permutation.

comparable in magnitude to the entries of the matrix Σ_{A_0} plotted against the permuted linear index $p^{\Sigma_{A_0}}(i_\ell)$. We also note that the entries of the matrix Ξ_k are smaller as the number of clusters increases because the optimization process changes less the original matrix A_0 . This indicates that the optimized matrices A_k do not differ from the original connectomes more than the uncertainty introduced by the measurement process. Bottom panels show that the square difference between the entries of the matrices A_0 and A_k distributes similarly to the entries of the matrix Σ_{A_0} , i.e., the higher the uncertainty of a specific weight, the larger the change introduced by the optimization algorithm. In this case, linear indices of both matrices are ordered according to the permutation $p^{\Sigma_{A_0}}$.

Stability analysis through MSF and heterogeneity

Figure 8 shows the results of the robustness analysis for all levels ℓ_k^* , along with the intervals of σ values for which the synchronous clusters for each level are stable according to the MSF approach (red lines). As expected, the average comparison measure \bar{B} between the target partition (derived from experimental data) and the partition obtained by simulating the network with the optimized and perturbed structural connectivity matrices A_k becomes lower as σ_A grows. It can be observed that \bar{B} is above the maximum value obtained by simulating the network with the original structural connectivity matrix A_0 in the large region enclosed within the yellow dashed curve. In this region, the optimized network (with connectivity matrix A_k) behaves in better accordance with the observed functional connectivity than the original network (with connectivity matrix A_0). Dark regions that fall outside the curve for low values of σ_A are always beyond the stability interval identified through the MSF approach. This indicates that our results are robust to perturbations on the connection weights, also comparing the numerical values of σ_A with the fact that the entries of A_k have a mean of 0.029 and a standard deviation of 0.065, with minimum 0 and maximum 0.952. The raster plots and BOLD signals corresponding to specific values of σ_A and \bar{B} (yellow dots in Fig. 8) are shown in Fig. 9: the progressive desynchronization of clusters is apparent in both the raster plots and the BOLD signals as σ_A increases and \bar{B} decreases.

A similar analysis was carried out by adding a white Gaussian noise term $\eta_i(t)$ with standard deviation σ_η to every node's excitatory subpopulation input (see Eq. (7) in Methods). In this case, network simulations are performed with a fixed-step explicit Euler method, with integration step $dt = 10^{-4}$. Panel a of Fig. 10 illustrates the results obtained for ℓ_{21}^* and strength $\sigma = 10^{-3}$: similarly, \bar{B} holds values close to 1 until $\sigma_\eta \leq 10^{-6}$. Note that \bar{B} is higher than the value obtained by simulating the network with A_0 for the same level and the same σ value, for standard deviation σ_η up to about 10^{-2} , which approaches the amplitude of the node input without noise; this means that the optimized structural connectivity matrix A_k appears to be in better accordance with the observed functional connectivity than A_0 , even for a relatively high noise level. This provides evidence of the robustness of the obtained results.

The robustness of the model was also tested by introducing heterogeneous node parameters. In particular, the model parameters that represent connection weights between inhibitory and excitatory subpopulations within each node (see Eq. (7) in Methods) were sampled from Gaussian distributions with standard deviation σ_w . Results are shown in panel b of Fig. 10: also in this scenario, the optimized structural connectivity matrix A_k is in better accordance with the observed functional connectivity than A_0 , up to about $\sigma_w = 5 \cdot 10^{-4}$.

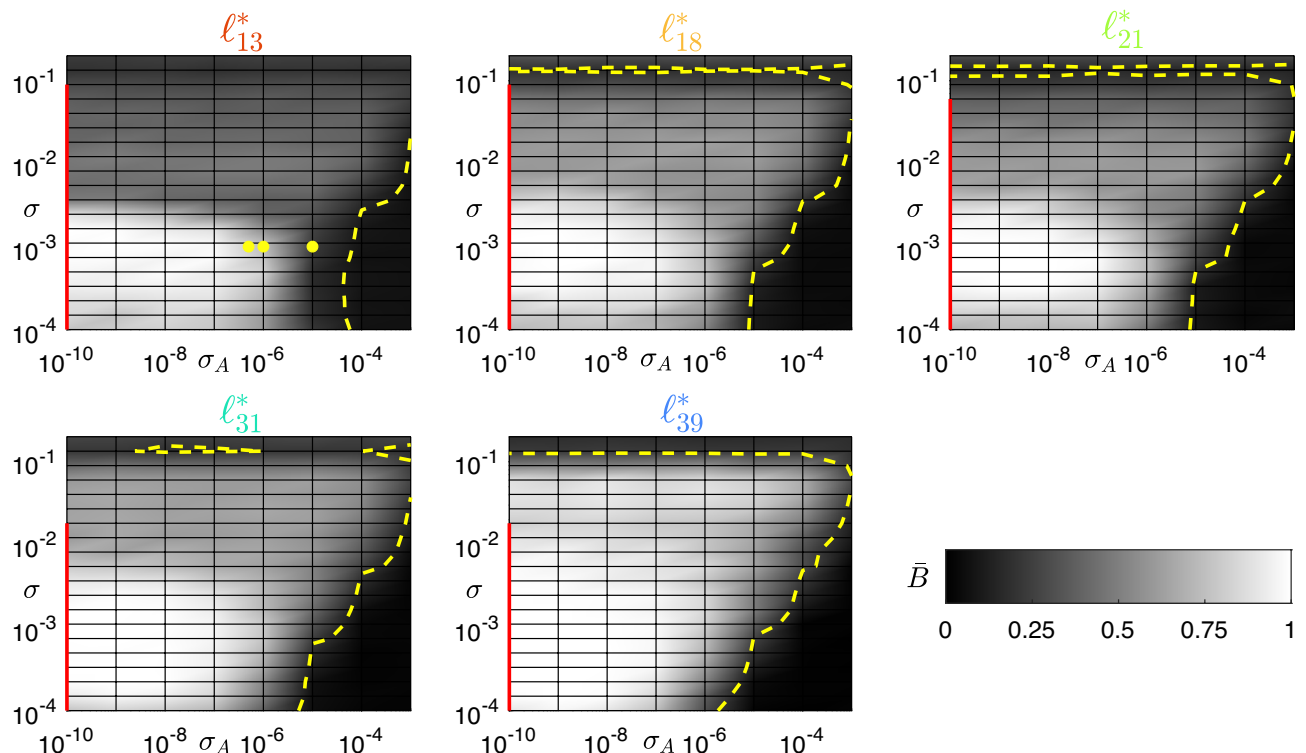


Figure 8. Comparison (through the average comparison measure \bar{B}) between the target cluster partition (derived from experimental data) and the partition obtained from network simulations with optimized matrices A_k perturbed by Gaussian noise, for each level ℓ_k^* ; σ_A on the abscissa denotes the noise standard deviation. Red bars on the vertical axis highlight the σ (synaptic strength) for which the synchronous clusters are stable according to the MSF approach. Dashed yellow lines are the level curves delimiting the regions where \bar{B} is higher than the maximum value obtained by simulating the network with the original structural connectivity matrix A_0 for the same level. Yellow dots mark the values of σ and σ_A used in Fig. 9.

Introducing delays

The delays τ_{ij} are calculated by multiplying an $N \times N$ distance matrix by a propagation velocity of 1.5 m/s⁶⁴; the distance matrix collects the pair-wise 3D euclidean distances between nodes, specifically between the centers of brain areas according to the HOA. Here, we quantize delays τ_{ij} over $L = 3$ values and carry out the optimization on A_0 and the subsequent analysis for ℓ_{21}^* . Our particular choice of $L = 3$ aims to keep the complexity limited, while still obtaining good results, as shown in the following. The optimization process is summarized in Fig. 11: the structural connectivity matrix A_0 is split into $L = 3$ matrices A_0^l , each corresponding to a coupling with delay τ^l . Each matrix A_0^l is optimized individually, thus obtaining matrices A_k^l , which are then summed to obtain the final optimized structural connectivity matrix $A_k = \sum_l A_k^l$.

Panel a of Fig. 12 shows that the entries of the matrix Ξ_k are still comparable with the entries of the matrix Σ_{A_0} , also considering $L = 3$ kinds of connections. Moreover, panel b shows that the square difference between the entries of the matrices A_0 and A_k distribute similarly to the entries of the matrix Σ_{A_0} .

The stability analysis through the MSF verified that the cluster synchronous solution for level ℓ_{21}^* is stable for $\sigma \in [10^{-4}, 0.1341]$, where 10^{-4} is the lowest value of σ that we considered. The raster plot for $\sigma = 10^{-3}$ and $L = 3$, with delays quantized as in panel a of Fig. 13, is shown in panel c, evidencing the synchronization between the nodes in each cluster. Heterogeneity in delay values was reintroduced *a posteriori* to test the robustness of the result obtained for $L = 3$. In particular, the delays were quantized over 50 values (panel b), which almost perfectly overlap with the original values of τ_{ij} ; we did not use the τ_{ij} values *as is*, because of the excessive computational burden. The corresponding raster plot is shown in panel d: as can be observed, heterogeneity in the delay values does not compromise the synchronization of the nodes within each cluster but influences the phase difference between clusters⁶⁵. This analysis evidences that, from a theoretical standpoint, the proposed method can be generalized to account for heterogeneous delays in the network; however, the computational cost of simulating the network dynamics for fully heterogeneous delays becomes prohibitive, since the computational cost of the MSF approach increases linearly with L .

Discussion

Neuroscientists monitor brain activity in several ways, using a variety of recording techniques in subjects under a plethora of health, neurophysiological and mental conditions. It becomes then important to integrate insights across diverse datasets to understand brain functions⁶⁶. In this paper, we have proposed a method that reconciles dMRI and fMRI data of a given subject by using an approach based on nonlinear dynamics and cluster

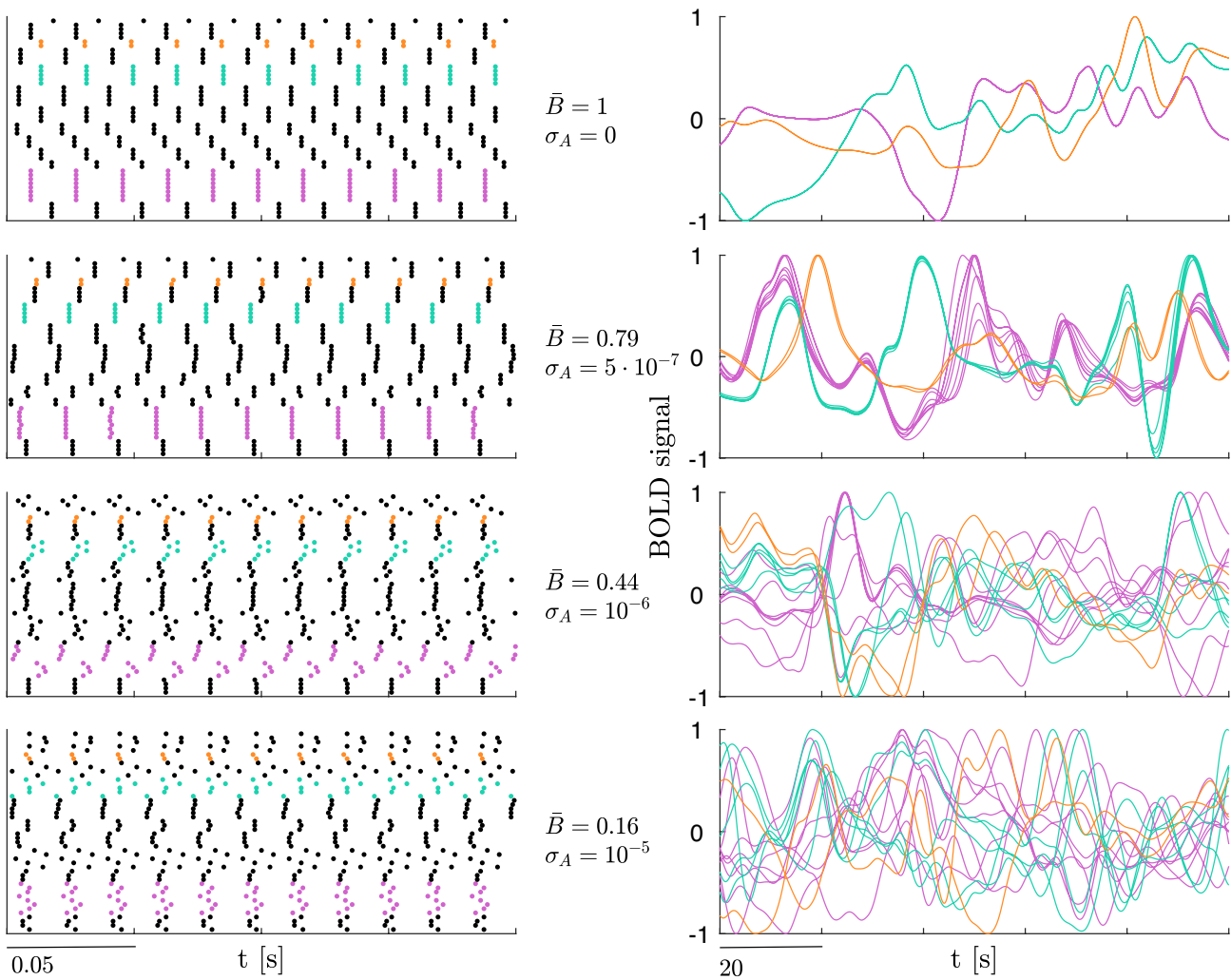


Figure 9. Raster plots (left) and normalized BOLD signals (right) for level ℓ_{13}^* , for different values of noise standard deviation σ_A and for fixed $\sigma = 10^{-3}$ (see yellow dots in Fig. 8). Points in the raster plots denote the peaks of excitatory subpopulation activity of each node, with nodes belonging to the same cluster represented as adjacent to each other. The normalized BOLD signals correspond to nodes in three sample clusters, chosen to showcase clusters of different sizes (pink: 8 nodes, teal: 5 nodes, orange: 2 nodes). Values of σ_A increase from top to bottom and correspond to decreasing values of \bar{B} .

synchronization. As a proof of concept, we have applied the proposed method to dMRI and fMRI recordings of a healthy adult subject at resting state. We first found that the original structural connectivity matrix was not compatible with the observed synchronous clusters of brain areas. By modifying the connectivity weights by an amount that is comparable with the uncertainty introduced by the measuring process, we obtained a network model that is able to reproduce the observed synchronous clusters, also in the presence of heterogeneity in the network. The proposed method may pave the way toward a better interplay of complex network principles and neurophysiological data.

It has been shown that synchronous electrophysiological activity of groups of neural populations underlies essential motor or cognitive processes in normal brain function⁶⁷. Moreover, abnormal synchronization of brain areas can be associated with a wide range of neurological and psychiatric disorders: in Parkinson's disease, abnormal synchronization of neural circuits in the cortex and basal ganglia can be observed⁶⁸, schizophrenia involves a disruption of neural synchrony⁶⁹, and epileptic seizures are characterized by excessive and synchronized electrical activity in the brain⁷⁰. Because of this, developing models that reproduce specific brain dynamics in terms of synchronized groups of brain areas, obtained by integrating structural and functional connectivity through cluster synchronization principles, is particularly relevant and could lead to a deeper understanding of brain functions.

While in the present paper we focused on a single hierarchical clustering for a given subject, we are aware that the study of dynamic functional connectivity reveals that brain activity switches between a set of states, where a finite number of clusterings are identifiable^{24,71}. Future work will focus on generalizing the proposed method by modifying the structural connectivity optimization process so that the optimized matrix admits multiple observed clusterings. The stability analysis could then be carried out for each synchronous cluster solution, and

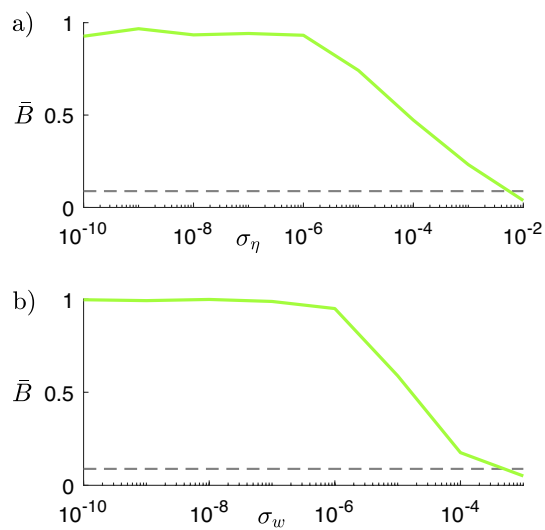


Figure 10. a) Comparison (through the average comparison measure \bar{B}) between the target cluster partition and the partition obtained from network simulations with connectivity matrix A_{21} and a white Gaussian noise term $\eta_i(t)$ added to every node's excitatory subpopulation input; the result is obtained for $\sigma = 10^{-3}$. σ_η is the noise signal standard deviation (see Eq. (7) in Methods). The gray dashed line marks the value of \bar{B} obtained by simulating the network with the original structural connectivity matrix A_0 and without noise for the same level and same σ value (see Fig. 6). b) Comparison (through the average comparison measure \bar{B}) between the target cluster partition and the partition obtained from network simulations with connectivity matrix A_{21} and heterogeneous nodes. Heterogeneity is introduced by sampling the parameters w_{EE} , w_{IE} , w_{EI} (see Eq. (7) in Methods) from Gaussian distributions with means $\mu_{w_{EE}} = 3.5$, $\mu_{w_{IE}} = 2.5$ and $\mu_{w_{EI}} = 3.75$ and standard deviation σ_w . The result is obtained for $\sigma = 10^{-3}$. The gray dashed line marks the value of \bar{B} obtained by simulating the network with the original structural connectivity matrix A_0 and homogeneous nodes for the same level and same σ value.

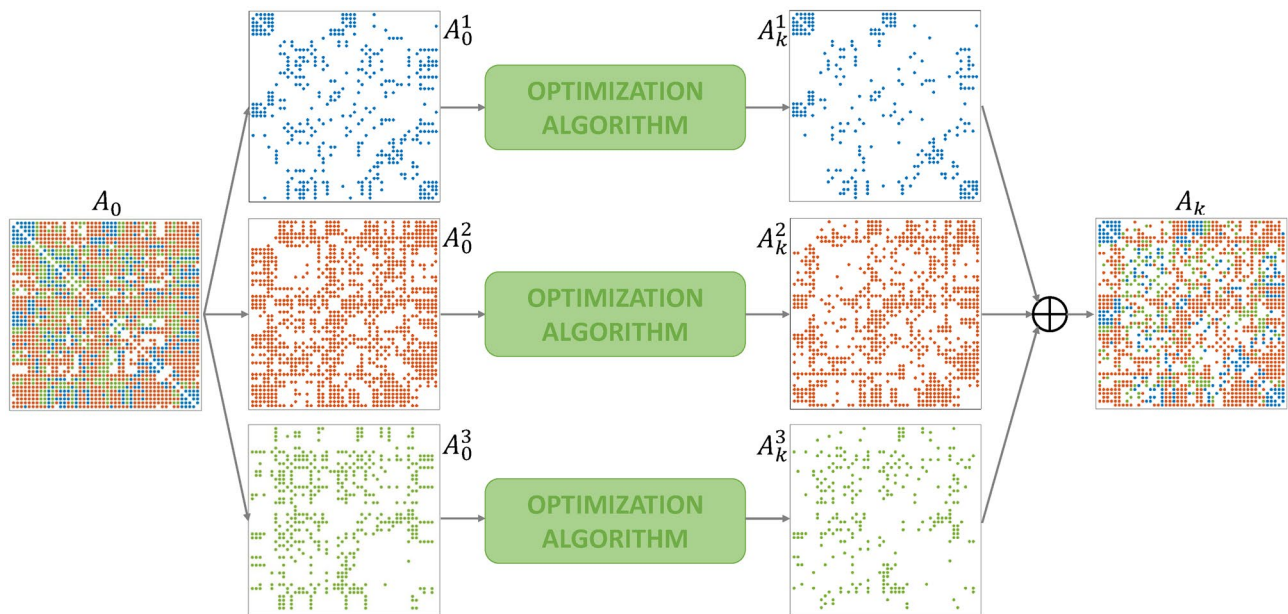


Figure 11. The structural connectivity matrix A_0 is split into 3 matrices A_0^1 , A_0^2 and A_0^3 , corresponding to link kinds with delay $\tau^1 = 0.0204$ s, $\tau^2 = 0.0518$ s and $\tau^3 = 0.0832$ s, respectively. In this example, $k = 21$.

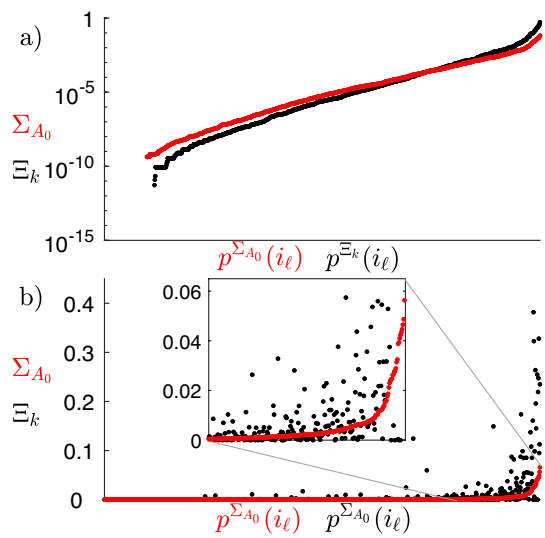


Figure 12. (a) Entries of the matrices Σ_{A_0} (red dots) and Ξ_k (black dots), for level ℓ_{21}^* , entries of both Σ_{A_0} and Ξ_k are displayed from the smallest to the largest and are plotted on a semi-logarithmic scale, with their linear indices i_ℓ ordered according to permutations $p^{\Sigma_{A_0}}$ and p^{Ξ_k} , respectively. (b) Entries of the matrices Σ_{A_0} (red dots) and Ξ_k (black dots), for level ℓ_{21}^* , entries of Σ_{A_0} are displayed on a linear scale from the smallest to the largest, with their linear indices i_ℓ ordered according to permutation $p^{\Sigma_{A_0}}$; entries of Ξ_k are displayed following the same permutation.

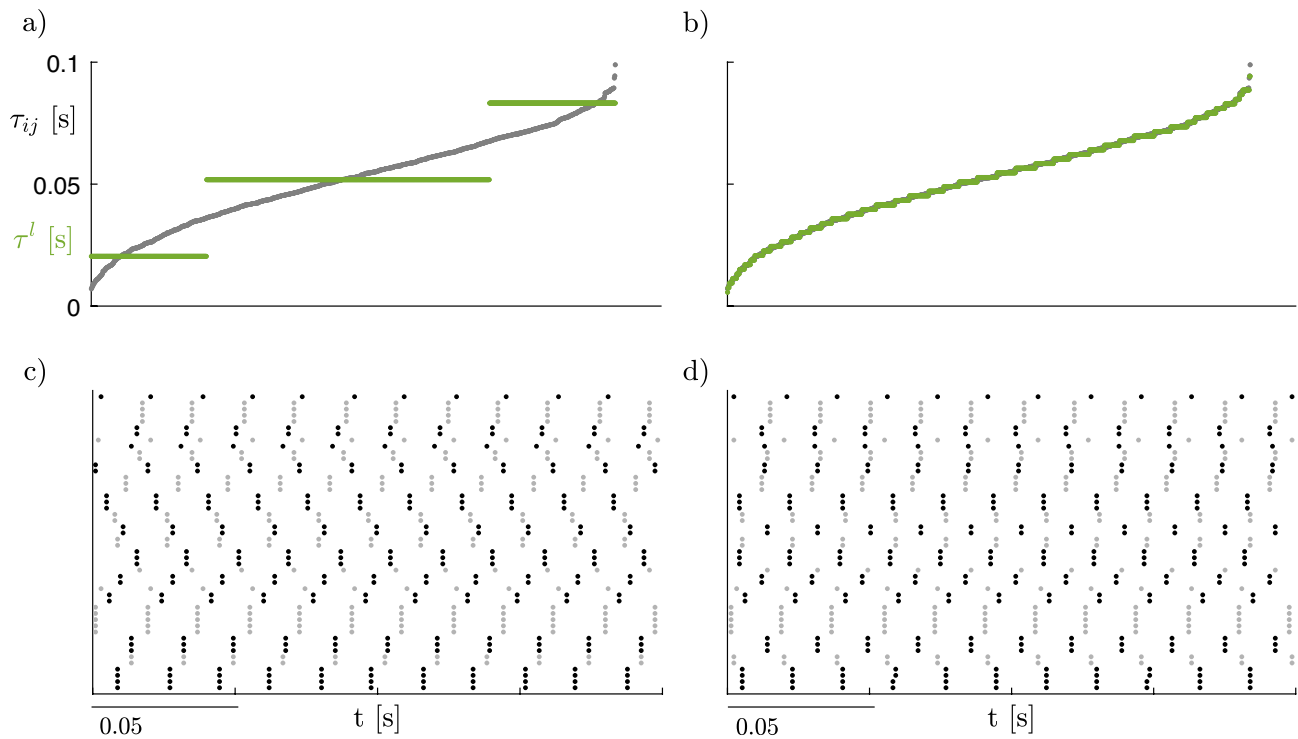


Figure 13. (a) Delays τ_{ij} sorted in ascending order (gray dots) and delays τ^l quantized over 3 values (green lines). (b) Delays τ_{ij} sorted in ascending order (gray dots) and delays τ^l quantized over 50 values (green lines). (c) Raster plot for level ℓ_{21}^* , for fixed $\sigma = 10^{-3}$ and delays quantized over 3 values. Points in the raster plots denote the peaks of the excitatory subpopulation activity of each node, with nodes belonging to the same cluster represented as adjacent to each other; clusters are represented by alternating black and gray colors to aid visualization. d) Raster plot for level ℓ_{21}^* , for fixed $\sigma = 10^{-3}$ and delays quantized over 50 values.

simulations with different initial conditions could give information on the basin of attraction of each one, thus providing a model able to fully reproduce the observed dynamic functional connectivity.

Differently from other model-based approaches, such as dynamic causal modeling⁷² or Multivariate Ornstein-Uhlenbeck processes⁷³, our approach does not aim at inferring effective connectivity, intended as a measure of the directional relationships in a dynamic model. In other words, we do not aim to generate a model able to retrace the spatiotemporal covariances of measured BOLD signals by inferring directed functional connections between nodes. Instead, we focus on reproducing the cluster synchronization observed among brain areas of a subject. The connections in our model are undirected and are heavily based on the measured structural connectivity: the small variations applied to the weights during the optimization process do not yield particular relevance from a neuroscientific point of view, and do not constitute a process of inference of unknown connections. These small variations, however, are enough to codify the balanced coloring condition in the structural connectivity matrix. This provides a network model that is strongly based on the physical connections and whose emergent dynamics exhibit the synchronous clusters observed in the functional connectivity of the subject. Notice that the proposed approach could nonetheless be generalized to asymmetric connectivity matrices detailing directed connections³⁰.

Next we discuss in deeper detail some key points of the proposed approach to evidence its flexibility. In the presented case study, we used functional and structural connectivity matrices where network nodes are regions of interest (ROIs) defined according to the HOA. Our method can however be applied independently of the anatomical atlas used, or even exploit functional and structural connectivity matrices where nodes are spatial brain components estimated by independent components analysis (ICA)^{74–76}, instead of ROIs. Moreover, functional connectivity matrices and the associated clustering could also be derived from other kinds of functional data (e.g. EEG, MEG)⁷⁷.

Hierarchical clustering is an established method to identify clusters of nodes in brain networks^{7,36–39}, due to the hierarchical modularity exhibited by the human brain⁷⁸. However, the identification of the most appropriate number of clusters from a dendrogram is not straightforward. We carried out a multi-level approach and selected the levels of interest ℓ_k^* based on considerations derived from the experimental data. We remark that the proposed method remains valid regardless of the nature of the identified clusters, which could also be defined on the basis of neuroscientifically relevant *a priori* knowledge such as known resting state networks, like the DMN. In the absence of multiple scans for each subject or with no *a priori* knowledge, it is also possible to use other metrics to determine the optimal number of clusters, such as the silhouette score⁷⁹ or the gap statistic⁸⁰. In principle, one could also consider all levels, but this would greatly increase the computational cost of the method. Moreover, if multiple scans are not available, we cannot obtain information on the variance of the structural connectivity matrices among sessions. In this case, this information is simply not included in the optimization process: vector α in Eq. (2) is simply defined as the stacked columns of matrix A_0 . In general, the cost function can be further customized, e.g., to impose that some elements of the connection matrix are not changed or to weigh differently the uncertainty about the entries of A_0 .

In the proposed example, nodal dynamics are described by the Wilson-Cowan NMM⁴⁴, with couplings as in^{5,81} and parameters as in⁸¹. In accordance with these and other studies^{82,83}, we only modeled long-range excitatory projections targeting excitatory sub-populations, since we do not have information regarding whether and which connections directly target inhibitory subpopulations. The direct contribution of the synaptic current to the inhibitory subpopulation could be taken into account by adding the term E_i^{syn} to the exponent of the second equation in Eq. system (7). Such modification of the Wilson-Cowan neural mass model would not alter the method proposed in the paper. Alternative models could also be employed, such as next-generation neural mass models, which exactly reproduce the macroscopic dynamics of heterogeneous spiking neural networks^{84–88}. This would allow the use of heterogeneous parameters identified with high precision. The MSF step can be taken provided that the considered neural mass model falls under the proposed formalism or the formalism is appropriately generalized. The node homogeneity hypothesis needed to carry out the optimization of the structural connectivity matrix and the stability analysis would require the use of average parameters, under the assumption that parameters of distinct brain areas are not too different⁸⁹. The proposed results have been obtained with data measured on healthy subjects in resting state. For non-healthy subjects, specific neural mass models should be used (e.g., the epileptor⁹⁰ for epilepsy, or the model proposed in⁹¹ for Parkinson's disease), but the proposed approach remains valid, *mutatis mutandis*. For healthy subjects exposed to a specific stimulus, an external input representing said stimulus could be added to the model. This would allow separating stimulus responses from ongoing activity⁹².

Methods

Definition of partition and coloring

Given a graph with N nodes, a partition $P = \{C_1, C_2, \dots, C_k\}$ of the graph is defined as a subdivision of its node set into k clusters, with cluster C_p composed of n_p nodes, $\sum_{p=1}^k n_p = N$ such that (i) there are no empty clusters, (ii) the clusters comprise all nodes and (iii) the clusters are pairwise disjoint. Each cluster can be identified through the labels of its constituting nodes and a given color. A network graph can admit many different colorings, each one describing a different partition.

Hierarchical clustering and similarity indices Ψ_1 and Ψ_2

Depending on the level $\ell \in \{1, \dots, N\}$ at which the dendrogram is cut horizontally, the corresponding clustering is described by the sub-trees originating from each branch cut by the horizontal line: for example, in Fig. 2 the red line cuts the dendrogram at the level corresponding to 13 clusters. For each level ℓ of the dendograms obtained from the hierarchical clustering of the correlation matrices, we calculate a cumulative (across sessions) similarity index Ψ_1 :

$$\Psi_1(\ell) = \frac{1}{N_s} \sum_{i=1}^{N_s} B_i(\ell) \quad (5)$$

where $B_i(\ell)$ is the comparison measure between a single pair of functional connectivity matrices (corresponding to different fMRI sessions on the same subject) and N_s is the total number of possible pairwise comparisons between the sessions; $B_i(\ell) = 1$ when two partitions are identical and $B_i(\ell) = 0$ when no pair of objects that appears in the same cluster in one partition is assigned to the same cluster in the other partition. We thus obtain N samples $\Psi_1(\ell)$. The clusters corresponding to each level ℓ_k^* are established by computing a second cumulative (across the selected levels) similarity index Ψ_2 for each session:

$$\Psi_2(s) = \frac{1}{M_\ell} \sum_{\mathcal{L}^*} \frac{1}{M_f} \sum_{i=1}^{M_f} B_i(s) \quad (6)$$

where $B_i(s)$ is the comparison measure between the partition in the current session s and the partition in session i .

Simulation procedure

1. We simulate the network dynamics and the corresponding BOLD signals for an array of values of σ (see Eq. (1)), and repeat the procedure n_{CI} times starting from different initial conditions chosen randomly.
2. For each simulation, we calculate the correlation matrix of the BOLD signals, discarding transient data. The resulting correlation matrix can be compared with the functional connectivity matrix X^* .
3. We apply the same hierarchical clustering that was applied on X^* on each of the calculated correlation matrices, thus obtaining M_ℓ clusterings with k clusters, each corresponding to the level ℓ_k^* . We compare each obtained partition with the target partition associated with X^* , and compute the Fowlkes and Mallows matching index averaged over the n_{CI} trials, which we denote as \bar{B} .

Wilson–Cowan neural mass model

The dynamics of the i -th node is described by the equations:

$$\begin{cases} \tau_E \dot{E}_i = -E_i + \frac{1}{1+e^{-c(w_{EE}E_i-w_{IE}I_i+P+\eta_i(t)+E_i^{syn}-\theta)}}, \\ \tau_I \dot{I}_i = -I_i + \frac{1}{1+e^{-c(w_{EI}E_i-\theta)}}, \end{cases} \quad (7)$$

with

$$E_i^{syn}(t) = \sigma \sum_j a_{ij} E_j(t - \tau_{ij}), \quad (8)$$

where the state variables $E_i(t)$ and $I_i(t)$ are the fraction of excitatory and inhibitory neurons firing per unit time at instant t , respectively; the weights w_{uv} , with $u, v = \{E, I\}$, describe the intra-population strength of connection from neuron type u to v ; c and θ are, respectively, the gain and the threshold of the sigmoid; P is a spontaneous excitatory background input; $\eta_i(t)$ is a white Gaussian noise signal, kept null unless otherwise stated; τ_E, τ_I control the timescales of the first-order kinetics; E_i^{syn} is the synaptic input to node i , which is determined by the structural connectivity matrix entries a_{ij} and the fraction of active excitatory cells in each j -th pre-synaptic population. Eq. (8) follows from the fact that long-range connections between cortical areas are only excitatory⁹³. Delays τ_{ij} are assigned to each connection between nodes i and j , i.e., to each entry of the structural connectivity matrix A_0 . We set the parameters as in⁸¹: $w_{EE} = 3.5$, $w_{IE} = 2.5$, $w_{EI} = 3.75$, $c = 4$, $\theta = 1$, $P = 0.34$. P is chosen so that the isolated node converges to an equilibrium point corresponding to a low activity state, but coupled nodes converge to limit cycles even for small coupling weights. A bifurcation diagram of the isolated node with respect to P is provided in the “Supplemental Material”, Note 3. Time constants are set to $\tau_E = 0.002$ s and $\tau_I = 0.004$ s, so that their ratio is as in⁸¹, but the nodes exhibit oscillations in the γ range (around 40 Hz) as in⁵.

For a fixed value of P , the convergence of the steady-state trajectory to a limit cycle or to an equilibrium point depends on the value of the synaptic input E_i^{syn} , which in turn is influenced by the overall strength of the connections σ in Eq. 8. In this paper, we consider the interval $\sigma \in [0.0001, 0.2]$, which yields oscillatory behavior of the nodes. For $\sigma > 0.2$ a growing portion of nodes ‘saturates’, converging to an equilibrium point, thus yielding constant $E_i(t)$ and $I_i(t)$ that are incompatible with the oscillating nature of the local field potential.

BOLD model

We calculate the BOLD signal for each node i by using the Balloon-Windkessel hemodynamic model of Friston and Harrison⁶⁰, which relates neural activity to perfusion changes. The model is described by the equations:

$$\begin{cases} \dot{s}_i = z_i - \kappa s_i - \gamma(f_i - 1), \\ \dot{f}_i = s_i, \\ \tau \dot{v}_i = f_i - v_i^{\frac{1}{\alpha}}, \\ \tau \dot{q}_i = f_i \frac{1-(1-\rho)f_i}{\rho} - v_i^{\frac{1}{\alpha}} \frac{q_i}{v_i}, \end{cases} \quad (9)$$

where s_i is the vasodilatory signal, which increases according to the neuronal activity z_i of the i -th region (in our case $z_i(t) = E_i(t) + I_i(t)$), and is subject to autoregulatory feedback; f_i is the inflow, v_i is the blood volume and q_i is the deoxyhemoglobin content. Parameter $\alpha = 0.32$ is the Grubb's exponent⁹⁴, $\rho = 0.34$ is the resting oxygen extraction fraction and the other biophysical parameters are set to $\kappa = 0.65$ per s, $\gamma = 0.41$ per s and $\tau = 0.98$ s, as per the mean values reported in⁶⁰.

The BOLD signal is taken to be a static nonlinear function of v_i and q_i :

$$y_i = V_0(7\rho(1 - q_i) + 2(1 - \frac{q_i}{v_i}) + (2\rho_i - 0.2)(1 - v_i)) \quad (10)$$

where $V_0 = 0.02$ is the resting blood volume fraction⁶⁰.

Master stability function

The cluster synchronization state obeys the following equation:

$$\dot{\mathbf{s}}_p(t) = \mathbf{F}(\mathbf{s}_p(t)) + \boldsymbol{\Gamma} \left(\mathbf{s}_p(t), \sigma \sum_l \sum_q r_{pq}^l \mathbf{G}(\mathbf{s}_q(t - \tau^l)) \right), \quad (11)$$

where the k -dimensional matrix $R^l = \{r_{pq}^l\}$ is the quotient matrix, such that $r_{pq}^l = \sum_{j \in \mathcal{C}_q} a_{ij}^l$ ($i \in \mathcal{C}_p$, $p, q = 1, 2, \dots, k$). We preliminarily define

$$D\tilde{\mathbf{F}}(\mathbf{s}_p(t)) = D\mathbf{F}(\mathbf{s}_p(t)) + D\boldsymbol{\Gamma}_1 \left(\mathbf{s}_p(t), \sigma \sum_l \sum_q r_{pq}^l \mathbf{G}(\mathbf{s}_q(t - \tau^l)) \right) \quad (12)$$

and

$$D\tilde{\boldsymbol{\Gamma}}_p = D\boldsymbol{\Gamma}_2 \left(\mathbf{s}_p(t), \sigma \sum_l \sum_q r_{pq}^l \mathbf{G}(\mathbf{s}_q(t - \tau^l)) \right), \quad (13)$$

where $D\mathbf{F}$ is the $m \times m$ Jacobian of the nodes' vector field and the m -dimensional matrix $D\boldsymbol{\Gamma}_1$ ($D\boldsymbol{\Gamma}_2$) is the derivative of $\boldsymbol{\Gamma}$ with respect to its first (second) argument. The linearized equations governing the dynamics of the perturbations about the synchronous solution $\mathbf{s}_p(t)$ can be written as:

$$\dot{\mathbf{w}}_i(t) = D\tilde{\mathbf{F}}(\mathbf{s}_p(t))\mathbf{w}_i(t) + D\tilde{\boldsymbol{\Gamma}}_p \sigma \sum_l \left[\sum_{q=1}^k D\mathbf{G}(\mathbf{s}_q(t - \tau^l)) \sum_{j \in \mathcal{C}_q} a_{ij}^l \mathbf{w}_j(t - \tau^l) \right] \quad (14)$$

Now we can rewrite Eqs. (14) in vector form by stacking all the state perturbation vectors together in one vector $\mathbf{W}(t)$. Moreover, we introduce the $N \times N$ diagonal matrix E_p , which is the cluster indicator matrix: E_p has entries $E_{p,ii} = 1$, if node $i \in \mathcal{C}_p$, 0 otherwise, i.e., this matrix identifies all the nodes i 's that belong to cluster \mathcal{C}_p . Therefore, we have:

$$\begin{aligned} \dot{\mathbf{W}}(t) &= \left[\sum_{p=1}^k E_p \otimes D\tilde{\mathbf{F}}(\mathbf{s}_p(t)) \right] \mathbf{W}(t) \\ &+ \left(\sum_{p=1}^k E_p \otimes D\tilde{\boldsymbol{\Gamma}}_p \right) \sigma \sum_l \left[\left(A^l \otimes I_n \sum_{q=1}^k E_q \otimes \mathbf{G}(\mathbf{s}_q(t - \tau^l)) \right) \mathbf{W}(t - \tau^l) \right] \end{aligned} \quad (15)$$

We compute the canonical transformation matrix T as the orthogonal matrix that simultaneously block-diagonalizes the matrices $A^1, A^2, \dots, A^L, E_1, E_2, \dots, E_C$ into D diagonal blocks, $T = \begin{pmatrix} T_{\parallel} \\ T_{\perp} \end{pmatrix} = SBD(A^1, A^2, \dots, A^L, E_1, E_2, \dots, E_C)$. Application of the matrix T yields $TA^lT^{-1} = \hat{A}^l$, where $\hat{A}^l = \hat{A}_{\parallel}^l \oplus \hat{A}_{\perp}^l = \bigoplus_{j=1}^D \hat{A}_j^l$. The symbol \oplus denotes the direct sum of matrices and the blocks \hat{A}_j^l $j = 1, 2, \dots, D$ have the same dimension. We remark that $\hat{A}_{\parallel}^l = \hat{A}_1^l$ and $\hat{A}_{\perp}^l = \bigoplus_{j=2}^D \hat{A}_j^l$. Moreover, we have that $TE_pT^{-1} = E_p$. By using matrix T , for the transverse perturbations we obtain,

$$\dot{\boldsymbol{\eta}}_{\perp}(t) = \underbrace{\left[\sum_{p=1}^k E_{p\perp} \otimes D\tilde{\mathbf{F}}(\mathbf{s}_p(t)) \right]}_{\rho_1(\{\mathbf{s}_p(t)\})} \boldsymbol{\eta}_{\perp}(t) \\ + \sum_l \underbrace{\left[\left(\sum_{p=1}^k E_{p\perp} \otimes D\tilde{\mathbf{F}}_p \right) \sigma \left(\hat{A}_{\perp}^l \otimes I_n \sum_{q=1}^k E_{q\perp} \otimes D\mathbf{G}(\mathbf{s}_q(t - \tau^l)) \right) \boldsymbol{\eta}_{\perp}(t - \tau^l) \right]}_{\rho_2^l(\{\mathbf{s}_p(t)\})}$$
(16)

where the block-diagonal matrix marked with \perp is a minor of the complete matrix $\hat{A}^l = TA^lT^{-1}$, containing only the blocks related to the transverse perturbations.

Data availability

The datasets analyzed during the current study are available in the “M2G: Reliable Human Connectomes At Scale” repository, <https://neurodata.io/mri/>.

Received: 1 June 2023; Accepted: 11 December 2023

Published online: 17 December 2023

References

- Gilson, M., Moreno-Bote, R., Ponce-Alvarez, A., Ritter, P. & Deco, G. Estimation of directed effective connectivity from fMRI functional connectivity hints at asymmetries of cortical connectome. *PLoS Comput. Biol.* **12**, e1004762 (2016).
- Bassett, D. S. *et al.* Reflections on the past two decades of neuroscience. *Nat. Rev. Neurosci.* **21**, 524–534 (2020).
- Liégeois, R., Santos, A., Matta, V., Van De Ville, D. & Sayed, A. H. Revisiting correlation-based functional connectivity and its relationship with structural connectivity. *Netw. Neurosci.* **4**, 1235–1251 (2020).
- Schilling, K. G. *et al.* Limits to anatomical accuracy of diffusion tractography using modern approaches. *Neuroimage* **185**, 1–11 (2019).
- Deco, G., Jirsa, V., McIntosh, A. R., Sporns, O. & Kötter, R. Key role of coupling, delay, and noise in resting brain fluctuations. *Proc. Natl. Acad. Sci.* **106**, 10302–10307 (2009).
- Sporns, O. The human connectome: a complex network. *Ann. N. Y. Acad. Sci.* **1224**, 109–125 (2011).
- Alexander-Bloch, A. *et al.* The discovery of population differences in network community structure: new methods and applications to brain functional networks in schizophrenia. *Neuroimage* **59**, 3889–3900 (2012).
- Bassett, D. S. & Sporns, O. Network neuroscience. *Nat. Neurosci.* **20**, 353–364 (2017).
- Sporns, O. & Bassett, D. S. New trends in connectomics. *Netw. Neurosci.* **2**(02), 125–127 (2018).
- Lynn, C. W. & Bassett, D. S. The physics of brain network structure, function and control. *Nat. Rev. Phys.* **1**, 318–332 (2019).
- Hahn, G. *et al.* Signature of consciousness in brain-wide synchronization patterns of monkey and human fMRI signals. *Neuroimage* **226**, 117470 (2021).
- Oswal, A. *et al.* Neural signatures of hyperdirect pathway activity in Parkinson’s disease. *Nat. Commun.* **12**, 1–14 (2021).
- Nowak, A. K., Vallacher, R. R., Praszkier, R., Rychwalska, A. & Zochowski, M. In Sync: The emergence of function in minds, groups and societies (Springer Nature, 2020).
- Shadlen, M. N. & Newsome, W. T. Noise, neural codes and cortical organization. *Curr. Opin. Neurobiol.* **4**, 569–579 (1994).
- Wang, X.-J. Neurophysiological and computational principles of cortical rhythms in cognition. *Physiol. Rev.* **90**, 1195–1268 (2010).
- Ponce-Alvarez, A. *et al.* Resting-state temporal synchronization networks emerge from connectivity topology and heterogeneity. *PLoS Comput. Biol.* **11**, e1004100 (2015).
- Suárez, L. E., Markello, R. D., Betzel, R. F. & Misić, B. Linking structure and function in macroscale brain networks. *Trends Cogn. Sci.* **24**, 302–315 (2020).
- Mišić, B. *et al.* Network-level structure-function relationships in human neocortex. *Cereb. Cortex* **26**, 3285–3296 (2016).
- Deligianidis, F., Carmichael, D. W., Zhang, G. H., Clark, C. A. & Clayden, J. D. Noddi and tensor-based microstructural indices as predictors of functional connectivity. *PLoS ONE* **11**, e0153404 (2016).
- Rosenthal, G. *et al.* Mapping higher-order relations between brain structure and function with embedded vector representations of connectomes. *Nat. Commun.* **9**, 2178 (2018).
- Avena-Koenigsberger, A., Misić, B. & Sporns, O. Communication dynamics in complex brain networks. *Nat. Rev. Neurosci.* **19**, 17–33 (2018).
- Deco, G., Jirsa, V. K. & McIntosh, A. R. Emerging concepts for the dynamical organization of resting-state activity in the brain. *Nat. Rev. Neurosci.* **12**, 43–56 (2011).
- Breakspear, M. Dynamic models of large-scale brain activity. *Nat. Neurosci.* **20**, 340–352 (2017).
- Cabral, J., Kringelbach, M. L. & Deco, G. Functional connectivity dynamically evolves on multiple time-scales over a static structural connectome: Models and mechanisms. *Neuroimage* **160**, 84–96 (2017).
- Honey, C. J. *et al.* Predicting human resting-state functional connectivity from structural connectivity. *Proc. Natl. Acad. Sci.* **106**, 2035–2040 (2009).
- Robinson, P., Sarkar, S., Pandejee, G. M. & Henderson, J. Determination of effective brain connectivity from functional connectivity with application to resting state connectivities. *Phys. Rev. E* **90**, 012707 (2014).
- Abdelnour, F., Dayan, M., Devinsky, O., Thesen, T. & Raj, A. Functional brain connectivity is predictable from anatomic network’s Laplacian Eigen-structure. *Neuroimage* **172**, 728–739 (2018).
- Sorrentino, F., Pecora, L. M., Hagerstrom, A. M., Murphy, T. E. & Roy, R. Complete characterization of the stability of cluster synchronization in complex dynamical networks. *Sci. Adv.* **2**, e1501737 (2016).
- Zhang, Y., Latora, V. & Motter, A. E. Unified treatment of synchronization patterns in generalized networks with higher-order, multilayer, and temporal interactions. *Commun. Phys.* **4**, 195 (2021).
- Lodi, M., Sorrentino, F. & Storace, M. One-way dependent clusters and stability of cluster synchronization in directed networks. *Nat. Commun.* **12**, 1–13 (2021).
- Moran, R., Pinotsis, D. A. & Friston, K. Neural masses and fields in dynamic causal modeling. *Front. Comput. Neurosci.* **7**, 57 (2013).
- Schaub, M. T. *et al.* Graph partitions and cluster synchronization in networks of oscillators. *Chaos: Interdiscipl. J. Nonlinear Sci.* **26**, 094821 (2016).

33. Siddique, A. B., Pecora, L., Hart, J. D. & Sorrentino, F. Symmetry-and input-cluster synchronization in networks. *Phys. Rev. E* **97**, 042217 (2018).
34. Pecora, L. M. & Carroll, T. L. Master stability functions for synchronized coupled systems. *Phys. Rev. Lett.* **80**, 2109 (1998).
35. Sporns, O. *Networks of the Brain*. (MIT Press, 2016).
36. Liu, X., Zhu, X.-H., Qiu, P. & Chen, W. A correlation-matrix-based hierarchical clustering method for functional connectivity analysis. *J. Neurosci. Methods* **211**, 94–102 (2012).
37. Wang, Y. & Li, T.-Q. Analysis of whole-brain resting-state fMRI data using hierarchical clustering approach. *PLoS ONE* **8**, e76315 (2013).
38. Warren, K. N. *et al.* Increased fMRI activity correlations in autobiographical memory versus resting states. *Hum. Brain Mapp.* **39**, 4312–4321 (2018).
39. Gotts, S. J., Gilmore, A. W. & Martin, A. Brain networks, dimensionality, and global signal averaging in resting-state fMRI: Hierarchical network structure results in low-dimensional spatiotemporal dynamics. *Neuroimage* **205**, 116289 (2020).
40. Fowlkes, E. B. & Mallows, C. L. A method for comparing two hierarchical clusterings. *J. Am. Stat. Assoc.* **78**, 553–569 (1983).
41. Golubitsky, M. & Stewart, I. Nonlinear dynamics of networks: the groupoid formalism. *Bull. Am. Math. Soc.* **43**, 305–364 (2006).
42. Sorrentino, F. & Pecora, L. Approximate cluster synchronization in networks with symmetries and parameter mismatches. *Chaos: Interdiscipl. J. Nonlinear Sci.* **26**, 094823 (2016).
43. Pecora, L. M., Sorrentino, F., Hagerstrom, A. M., Murphy, T. E. & Roy, R. Cluster synchronization and isolated desynchronization in complex networks with symmetries. *Nat. Commun.* **5**, 1–8 (2014).
44. Wilson, H. R. & Cowan, J. D. Excitatory and inhibitory interactions in localized populations of model neurons. *Biophys. J.* **12**, 1–24 (1972).
45. Uhlig, F. Simultaneous block diagonalization of two real symmetric matrices. *Linear Algebra Appl.* **7**, 281–289 (1973).
46. Maehara, T. & Murota, K. A numerical algorithm for block-diagonal decomposition of matrix $*$ -algebras with general irreducible components. *Jpn. J. Ind. Appl. Math.* **27**, 263–293 (2010).
47. Murota, K., Kanno, Y., Kojima, M. & Kojima, S. A numerical algorithm for block-diagonal decomposition of matrix $*$ -algebras with application to semidefinite programming. *Jpn. J. Ind. Appl. Math.* **27**, 125–160 (2010).
48. Zhang, Y. & Motter, A. E. Symmetry-independent stability analysis of synchronization patterns. *SIAM Rev.* **62**, 817–836 (2020).
49. Panahi, S., Klickstein, I. & Sorrentino, F. Cluster synchronization of networks via a canonical transformation for simultaneous block diagonalization of matrices. *Chaos: Interdiscipl. J. Nonlinear Sci.* **31**, 111102 (2021).
50. Cho, Y. S., Nishikawa, T. & Motter, A. E. Stable chimeras and independently synchronizable clusters. *Phys. Rev. Lett.* **119**, 084101 (2017).
51. MRI Cloud. <https://neurodata.io/mri/>. Accessed 21 July 2022.
52. Kiar, G. *et al.* A high-throughput pipeline identifies robust connectomes but troublesome variability. *bioRxiv* 188706 (2018).
53. Zuo, X.-N. *et al.* An open science resource for establishing reliability and reproducibility in functional connectomics. *Sci. Data* **1**, 1–13 (2014).
54. Coluzzi, D. *et al.* Development and testing of spider-net: An interactive tool for brain connectogram visualization, sub-network exploration and graph metrics quantification. *Front. Neurosci.* **16**, 818385 (2022).
55. Raichle, M. E. *et al.* A default mode of brain function. *Proc. Natl. Acad. Sci.* **98**, 676–682 (2001).
56. Greicius, M. D., Krasnow, B., Reiss, A. L. & Menon, V. Functional connectivity in the resting brain: A network analysis of the default mode hypothesis. *Proc. Natl. Acad. Sci.* **100**, 253–258 (2003).
57. Buckner, R. L., Andrews-Hanna, J. R. & Schacter, D. L. The brain's default network: Anatomy, function, and relevance to disease. *Ann. N. Y. Acad. Sci.* **1124**, 1–38 (2008).
58. Finotelli, P. *et al.* Exploring resting-state functional connectivity invariants across the lifespan in healthy people by means of a recently proposed graph theoretical model. *PLoS ONE* **13**, e0206567 (2018).
59. Finotelli, P., Piccardi, C., Miglio, E. & Dulio, P. A graphlet-based topological characterization of the resting-state network in healthy people. *Front. Neurosci.* **15**, 665544 (2021).
60. Friston, K. J., Harrison, L. & Penny, W. Dynamic causal modelling. *Neuroimage* **19**, 1273–1302 (2003).
61. Jeurissen, B., Descoteaux, M., Mori, S. & Leemans, A. Diffusion MRI fiber tractography of the brain. *NMR Biomed.* **32**, e3785 (2019).
62. O'Donnell, L. J. & Pasternak, O. Does diffusion MRI tell us anything about the white matter? An overview of methods and pitfalls. *Schizophr. Res.* **161**, 133–141 (2015).
63. Jones, D. K., Knötsche, T. R. & Turner, R. White matter integrity, fiber count, and other fallacies: The do's and don'ts of diffusion MRI. *Neuroimage* **73**, 239–254 (2013).
64. Shimono, M. & Hatano, N. Efficient communication dynamics on macro-connectome, and the propagation speed. *Sci. Rep.* **8**, 1–15 (2018).
65. Panchuk, A., Rosin, D. P., Hövel, P. & Schöll, E. Synchronization of coupled neural oscillators with heterogeneous delays. *Int. J. Bifurc. Chaos* **23**, 1330039 (2013).
66. Ranade, S. A common voice for neural data. *Nat. Neurosci.* **25**, 1583 (2022).
67. Ward, L. M. Synchronous neural oscillations and cognitive processes. *Trends Cogn. Sci.* **7**, 553–559 (2003).
68. Ahn, S., Zuber, S. E., Worth, R. M., Witt, T. & Rubchinsky, L. L. Interaction of synchronized dynamics in cortex and basal ganglia in Parkinson's disease. *Eur. J. Neurosci.* **42**, 2164–2171 (2015).
69. Zhu, J. *et al.* Abnormal synchronization of functional and structural networks in schizophrenia. *Brain Imaging Behav.* **14**, 2232–2241 (2020).
70. Farahmand, S., Sobayo, T. & Mogul, D. J. Noise-assisted multivariate EMD-based mean-phase coherence analysis to evaluate phase-synchrony dynamics in epilepsy patients. *IEEE Trans. Neural Syst. Rehabil. Eng.* **26**, 2270–2279 (2018).
71. Preti, M. G., Bolton, T. A. & Van De Ville, D. The dynamic functional connectome: State-of-the-art and perspectives. *Neuroimage* **160**, 41–54 (2017).
72. Friston, K. J., Kahan, J., Biswal, B. & Razi, A. A DCM for resting state fMRI. *Neuroimage* **94**, 396–407 (2014).
73. Gilson, M. *et al.* Model-based whole-brain effective connectivity to study distributed cognition in health and disease. *Netw. Neurosci.* **4**, 338–373 (2020).
74. Wu, L. & Calhoun, V. Joint connectivity matrix independent component analysis: Auto-linking of structural and functional connectivities. *Hum. Brain Mapp.* **44**, 1533–1547 (2023).
75. Smith, S. M. *et al.* Network modelling methods for fMRI. *Neuroimage* **54**, 875–891 (2011).
76. Marrelec, G. & Fransson, P. Assessing the influence of different ROI selection strategies on functional connectivity analyses of fMRI data acquired during steady-state conditions. *PLoS ONE* **6**, e14788 (2011).
77. Cabral, J. *et al.* Metastable oscillatory modes emerge from synchronization in the brain spacetime connectome. *Commun. Phys.* **5**, 1–13 (2022).
78. Meunier, D., Lambiotte, R., Fornito, A., Ersche, K. & Bullmore, E. T. Hierarchical modularity in human brain functional networks. *Front. Neuroinform.* **3**, 37 (2009).
79. Rousseeuw, P. J. Silhouettes: A graphical aid to the interpretation and validation of cluster analysis. *J. Comput. Appl. Math.* **20**, 53–65 (1987).

80. Tibshirani, R., Walther, G. & Hastie, T. Estimating the number of clusters in a data set via the gap statistic. *J. R. Stat. Soc.: Series B (Stat. Methodol.)* **63**, 411–423 (2001).
81. Abeysuriya, R. G. *et al.* A biophysical model of dynamic balancing of excitation and inhibition in fast oscillatory large-scale networks. *PLoS Comput. Biol.* **14**, e1006007 (2018).
82. Hellyer, P. J., Jachs, B., Clopath, C. & Leech, R. Local inhibitory plasticity tunes macroscopic brain dynamics and allows the emergence of functional brain networks. *Neuroimage* **124**, 85–95 (2016).
83. Daffertshofer, A. & van Wijk, B. C. On the influence of amplitude on the connectivity between phases. *Front. Neuroinform.* **5**, 6 (2011).
84. Luke, T. B., Barreto, E. & So, P. Complete classification of the macroscopic behavior of a heterogeneous network of theta neurons. *Neural Comput.* **25**, 3207–3234 (2013).
85. Laing, C. R. Derivation of a neural field model from a network of theta neurons. *Phys. Rev. E* **90**, 010901 (2014).
86. Montbrió, E., Pazó, D. & Roxin, A. Macroscopic description for networks of spiking neurons. *Phys. Rev. X* **5**, 021028 (2015).
87. Coombes, S. & Byrne, Á. Next generation neural mass models. In *Nonlinear Dynamics in Computational Neuroscience*, 1–16 (Springer, 2019).
88. Taher, H., Torcini, A. & Olmi, S. Exact neural mass model for synaptic-based working memory. *PLoS Comput. Biol.* **16**, e1008533 (2020).
89. Deco, G., Kringselbach, M. L., Jirsa, V. K. & Ritter, P. The dynamics of resting fluctuations in the brain: Metastability and its dynamical cortical core. *Sci. Rep.* **7**, 1–14 (2017).
90. Chizhov, A. V., Zefirov, A. V., Amakhin, D. V., Smirnova, E. Y. & Zaitsev, A. V. Minimal model of interictal and ictal discharges epileptor-2. *PLoS Comput. Biol.* **14**, e1006186 (2018).
91. Liu, F. *et al.* A neural mass model of basal ganglia nuclei simulates pathological beta rhythm in Parkinson's disease. *Chaos: Interdiscipl. J. Nonlinear Sci.* **26**, 123113 (2016).
92. Filipchuk, A., Schwenkgrub, J., Destexhe, A. & Bathellier, B. Awake perception is associated with dedicated neuronal assemblies in the cerebral cortex. *Nat. Neurosci.*, 1–12 (2022).
93. Bittner, S. R. *et al.* Population activity structure of excitatory and inhibitory neurons. *PLoS ONE* **12**, e0181773 (2017).
94. Grubb, R. L. Jr., Raichle, M. E., Eichling, J. O. & Ter-Pogossian, M. M. The effects of changes in PaCO₂ cerebral blood volume, blood flow, and vascular mean transit time. *Stroke* **5**, 630–639 (1974).

Acknowledgements

The authors would like to express their sincere appreciation to Maurizio Mattia for reading the first version of this manuscript and providing constructive comments.

Author contributions

F.S. and M.S. designed and supervised the research; V.B. and M.L. performed the research; V.B., M.L., F.S., and M.S. analyzed the data and interpreted the results; V.B. and M.S. wrote and revised the manuscript; M.L. and F.S. contributed to writing and revised the manuscript.

Competing interests

The authors declare no competing interests.

Additional information

Supplementary Information The online version contains supplementary material available at <https://doi.org/10.1038/s41598-023-49746-2>.

Correspondence and requests for materials should be addressed to M.S.

Reprints and permissions information is available at www.nature.com/reprints.

Publisher's note Springer Nature remains neutral with regard to jurisdictional claims in published maps and institutional affiliations.



Open Access This article is licensed under a Creative Commons Attribution 4.0 International License, which permits use, sharing, adaptation, distribution and reproduction in any medium or format, as long as you give appropriate credit to the original author(s) and the source, provide a link to the Creative Commons licence, and indicate if changes were made. The images or other third party material in this article are included in the article's Creative Commons licence, unless indicated otherwise in a credit line to the material. If material is not included in the article's Creative Commons licence and your intended use is not permitted by statutory regulation or exceeds the permitted use, you will need to obtain permission directly from the copyright holder. To view a copy of this licence, visit <http://creativecommons.org/licenses/by/4.0/>.

© The Author(s) 2023